






## Article

# Classification of Fungal Pigments by Simulating Their Optical Properties Using Evolutionary Optimization

Roman Y. Pishchalnikov <sup>1,\*</sup>, Denis D. Chesalin <sup>1</sup>, Vasily A. Kurkov <sup>1,2</sup>, Andrei P. Razjivin <sup>3</sup>, Sergey V. Gudkov <sup>1,4,5</sup>, Andrey A. Grishin <sup>4</sup>, Alexey S. Dorokhov <sup>4</sup> and Andrey Yu. Izmailov <sup>4</sup>

- <sup>1</sup> Prokhorov General Physics Institute of the Russian Academy of Sciences, 119991 Moscow, Russia; genoa-and-pittsburgh@mail.ru (D.D.C.); v.k27@yandex.ru (V.A.K.); s\_makariy@rambler.ru (S.V.G.)  
<sup>2</sup> Moscow Institute of Physics and Technology (National Research University), 141701 Dolgoprudny, Russia  
<sup>3</sup> Belozersky Research Institute of Physico-Chemical Biology, Moscow State University, 119992 Moscow, Russia; razjivin@gmail.com  
<sup>4</sup> Federal State Budgetary Scientific Institution “Federal Scientific Agroengineering Center VIM” (FSAC VIM), 109428 Moscow, Russia; 5145412@mail.ru (A.A.G.); dorokhov@rgau-msha.ru (A.S.D.); vim@vim.ru (A.Y.I.)  
<sup>5</sup> Institute of Biology and Biomedicine, Lobachevsky State University of Nizhny Novgorod, 603022 Nizhny Novgorod, Russia  
\* Correspondence: rpishchal@kapella.gpi.ru

**Abstract:** Modern developments in data analysis techniques and evolutionary optimization algorithms have made it possible to analyze large amounts of unstructured digital data sets. Based on the differential evolution algorithm and semiclassical quantum simulations, we have recently proposed a method for classifying and analyzing the optical properties of organic pigments. In this paper, we present the results of modeling the absorption spectra of five carotenoids synthesized during the vital activity of the ascomycetous fungi: neurosporaxanthin, neurosporene, torulene,  $\gamma$ -carotene, and  $\zeta$ -carotene. We calculated the absorption spectra for each pigment using the multimode Brownian oscillator theory, which allows us to evaluate the influence of molecular vibrations on the electronic transitions in the pigment. We applied a generalized spectral density function method to our modeling, taking into account the contributions of 13 vibrational modes with frequencies varying between  $100\text{ cm}^{-1}$  and  $3000\text{ cm}^{-1}$ . This approach allowed us to gain a deeper understanding of how molecular vibrations affect the absorption spectra of these organic compounds. Thus, each absorption spectrum was associated with a unique set of Huang–Rhys factors (which represent the effective electron–phonon interaction). This set can be considered as a kind of “fingerprint” that characterizes the optical response of the pigment in the solvent.

**Keywords:** absorption; neurosporaxanthin; neurosporene; torulene;  $\gamma$ -carotene;  $\zeta$ -carotene; Fusarium fungi; optimization; multimode Brownian oscillator model; differential evolution

**MSC:** 68W50; 81V55; 81Q20



**Citation:** Pishchalnikov, R.Y.; Chesalin, D.D.; Kurkov, V.A.; Razjivin, A.P.; Gudkov, S.V.; Grishin, A.A.; Dorokhov, A.S.; Izmailov, A.Y. Classification of Fungal Pigments by Simulating Their Optical Properties Using Evolutionary Optimization. *Mathematics* **2024**, *12*, 3844. <https://doi.org/10.3390/math12233844>

Academic Editor: Ioannis Tsoulos

Received: 19 October 2024

Revised: 27 November 2024

Accepted: 2 December 2024

Published: 5 December 2024



**Copyright:** © 2024 by the authors. Licensee MDPI, Basel, Switzerland. This article is an open access article distributed under the terms and conditions of the Creative Commons Attribution (CC BY) license (<https://creativecommons.org/licenses/by/4.0/>).

## 1. Introduction

Assessment of the degree of infection in grain crops at the early stages of disease development, when external signs are not yet visually manifested, is a primary task of monitoring product quality [1]. The most practical way to analyze the condition of the outer surface of grains non-invasively and quickly is through the use of spectroscopic data in the visible and ultraviolet ranges [2], particularly absorption spectra, which can be recorded and automated to the maximum extent possible. Photosynthetic membranes of higher plants, bacteria, and algae [3], as well as fungal hyphae, contain different types of organic pigments that absorb and emit light quanta in the visible range [4,5]. Therefore, it seems that using various spectroscopic techniques, such as measurement of absorption, fluorescence [6,7], and Raman spectra [8,9], can easily solve the problem of identifying

the samples under study. However, there are several reasons why a straightforward interpretation of experimental data is not always reliable. Firstly, the pigment composition of photosynthetic organisms remains stable during development, while most fungi have a different pigment composition at each stage of growth [10–14]. Secondly, the optical properties of pigments, especially carotenoids, can vary significantly depending on the environment, making it difficult to identify them accurately [15,16]. One possible solution to this problem is to use a numerical simulation to analyze the spectra obtained from experiments. By comparing theoretical and experimental data, researchers can use the effective optimization algorithm to distinguish the specific optical response of individual pigments from the overall signal. This approach would allow for the detection of infections based on the presence or absence of certain pigments.

The optical activity of biopigments in the visible spectral range is associated with the singlet electronic transitions from the ground to excited states [17]. For instance, the absorption spectrum of carotenoids between 350 and 500 nm corresponds to an optically allowed  $|S_0\rangle \rightarrow |S_2\rangle$  electronic transition [18,19]. Depending on the strength of the interaction between this electronic transition and the vibrations of the molecular skeleton, the lineshape of the spectra of this transition can vary from a well-defined three-band pattern to that of a broad one-band [20]. Semiclassical quantum theory [21], which describes the interaction between radiation and matter, allows us to quantitatively estimate the optical response of a system based on the two-particle correlation function of the electronic transition moment [22]. Eventually, the absorption spectrum is determined by a set of effective parameters that characterize the vibrational modes of a given system [23,24]. Most importantly, these parameters can be estimated only by simulation of the experimental data [25].

Obviously, in order to accurately fit the experimental spectra and obtain statistically significant values for model parameters, optimization algorithms must be used [16,26]. Currently, the most effective algorithms are those that are nature inspired and evolutionary [27–29], such as the genetic algorithm (GA) [30], particle swarm optimization [31], and differential evolution (DE) [32,33]. These algorithms allow us to minimize the target function with a large number of parameters, regardless of the type of problems being addressed [34]. A notable example of using the GA to model the optical response of biomolecules and proteins is the analysis of spectroscopic data obtained from photosynthetic pigment–protein complexes. This includes simulating the dynamics of excited electronic states in photosystem I [35], studying the triplet states in the reaction center of photosystem II [36], calculating the characteristics of the linear optical response of the light-harvesting complex II from higher plants [37], and modeling linear spectroscopy of monomeric photosystem I from cyanobacteria [38]. The DE algorithm is widely used in various engineering applications [32,33,39]. However, when compared with the GA, the DE algorithm may be more suitable for modeling using semiclassical quantum theory. The classical version of DE includes a set of strategies for estimating mutant vectors, which allows it to tune for maximum performance without additional modifications to the algorithm for most applied problems. The successful implementation of this algorithm for optimizing semiclassical quantum calculations has been demonstrated in a series of papers published by our laboratory on the theoretical investigation of photosynthetic pigment spectroscopy [1,15,16].

The use of DE to model experimental spectra of organic pigments has demonstrated that the potential of evolutionary optimization extends beyond simple spectrum fitting [16]. In fact, the combined use of DE optical response simulation procedures allows us to analyze the physical mechanisms underlying the characteristic intensities of interactions between electronic excitations and vibrations of pigment molecules at different frequencies. Recently, we have proposed a method for the modeling of optical responses of the pigments with DE based on the concept of generalized spectral density [15]. This approach allows us to calculate the absorption spectra of electronic transitions for any pigment whose optical response in the visible range can be measured. Furthermore, it is not necessary to know the

exact set of vibrational modes in advance. The initial function of the generalized spectral density is evaluated based on a comb of frequencies for which the effective electron–phonon interactions (Huang–Rhys factors) have not been determined and are adjusted during the optimization process [15].

In this study, we have further improved our method by modifying the spectral density formula. Firstly, the damping factor for each vibrational mode was made dependent on its frequency, so that their values decrease as the mode frequency increases. This means that the lowest frequency mode ( $100\text{ cm}^{-1}$ ) is strongly overdamped. This type of spectral density allows us to more accurately take into account the influence of the solvent or protein environment on the pigment. Secondly, the DE settings were optimized for the specific problem being solved. Based on our previous experience [15,16], we realized that even if the minimized function did not actually change, some model parameters could still remain highly variable for a long time. Therefore, the evolution process was extended to almost double its original duration in order to ensure a complete stop in the variation in the model parameters.

Five spectra of neurosporaxanthin, neurosporene, torulene,  $\gamma$ -carotene, and  $\zeta$ -carotene in acetone (Figure 1) were used to demonstrate the performance of our method. Experimental data measured at room temperature were taken from a study aiming to trace the biosynthetic steps of neurosporaxanthin and its precursors [40] in ascomycete fungi since, in addition to a representative group of polyketides [41–43], carotenoids are also indicators of certain stages of fungal growth [44,45]. The ability to distinguish their optical responses in different environments (polar and non-polar solvents, proteins) will make it possible to develop the methods for the detection of infections in agricultural crops at early stages of germination.

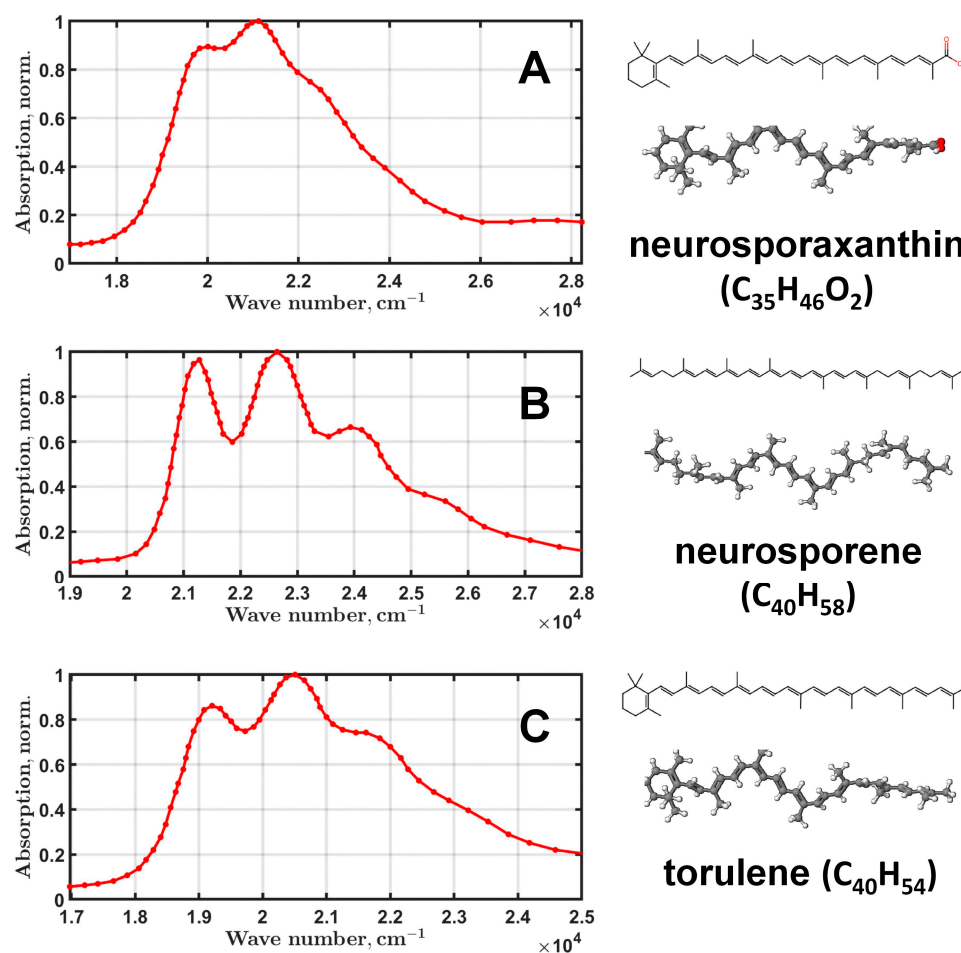
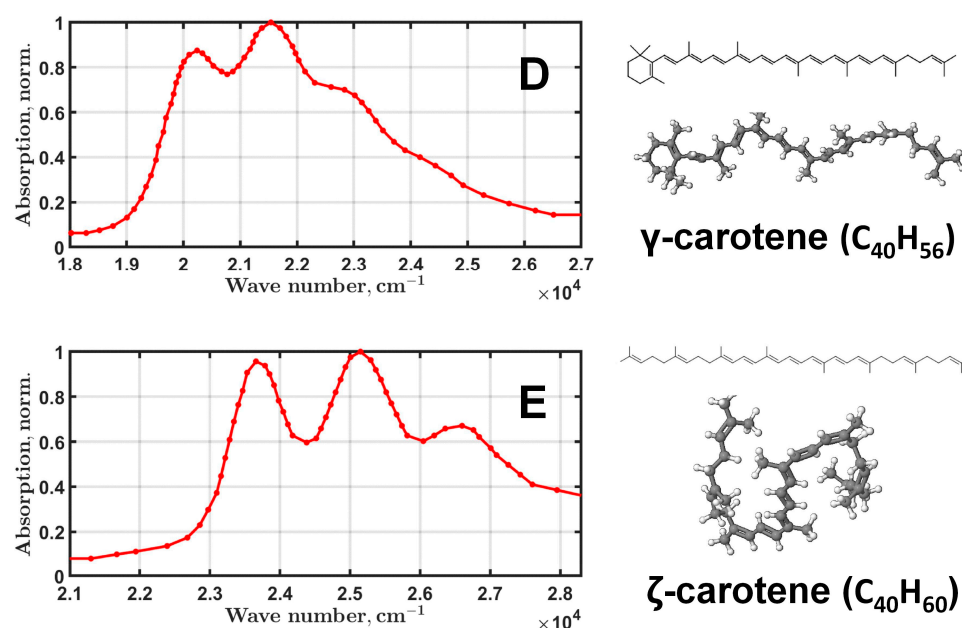


Figure 1. Cont.



**Figure 1.** Absorption spectra and chemical structures of neurosporaxanthin (A), neurosporene (B), torulene (C), γ-carotene (D), and ζ-carotene (E). Data taken from [40].

The remainder of this paper is structured as follows: Section 2 provides a brief overview of the physical theory and optimization algorithms used in the study. Section 3 presents the obtained results. Section 4 discusses the details of the results and their implications. Finally, Section 5 concludes with a summary of the findings.

## 2. Materials and Methods

### 2.1. Theory

To understand the process of light quanta absorption by a system of electronic states and to simulate the optical response, one can employ the semiclassical theory of interaction between the matter and electromagnetic field. In this case, the key element of the calculations is the Hamiltonian of the system,  $H_{sys}$ , which represents the total energy of electronic and vibrational states. If we consider a two-level system consisting of a ground state and an excited state that are coupled to a set of vibrational modes, the Hamiltonian for the ground state  $H_g$  and the excited state  $H_e$  can be expressed as follows:

$$H_{sys} = H_g + H_e, \quad (1)$$

$$H_g = \sum_j \left( \frac{p_j^2}{2m_j} + \frac{1}{2} m_j \omega_j^2 q_j^2 \right), \quad (2)$$

$$H_e = \hbar \Omega_{eg}^0 + \sum_j \left[ \frac{p_j^2}{2m_j} + \frac{1}{2} m_j \omega_j^2 (q_j - d_j)^2 \right], \quad (3)$$

where  $p_j, m_j, q_j, d_j$  are the effective moments, masses, coordinates, and displacements for each  $j$ th mode, respectively.  $\hbar \Omega_{eg}^0$  is the energy gap between the electronic states.

To simulate the absorption spectrum of the system described by (1), it is necessary to calculate the first order polarization:

$$P^{(1)}(r, t) = \int_0^\infty dt_1 S^{(1)}(t_1) E(r, t - t_1) + c.c., \quad (4)$$



where c.c. stands for the complex conjugate and  $S^{(1)}(t_1)$  is the linear response function. This function can be calculated by evaluating the correlation function of the electronic transition dipole moment between the ground and excited states:

$$S^{(1)}(t_1) = \frac{i}{\hbar} \theta(t_1) (\langle V(t_1) V(0) \rho(-\infty) \rangle - \langle V(0) V(t_1) \rho(-\infty) \rangle) \quad (5)$$

where  $\rho(-\infty)$  represents the matrix operator of equilibrium density,  $\theta(t_1)$  is the Heaviside step function, and  $V(t_1)$  is the interaction dipole operator.

In general, the knowledge of the linear response function is sufficient to calculate the absorption spectrum for a two-level system:

$$\sigma_{abs}(\omega) = \int_{-\infty}^{\infty} dt S^{(1)}(t_1) e^{i\omega t}, \quad (6)$$

$$S^{(1)}(t_1) = \frac{i}{\hbar} \theta(t_1) e^{-i\omega_{eg}t_1 - g(t_1)} + c.c., \quad (7)$$

$$g(t) = \int_0^t d\tau_2 \int_0^{\tau_2} d\tau_1 C(\tau_1), \quad (8)$$

where  $g(t)$  is the lineshape function and  $C(t)$  is a generalized expression for the transition moment correlation function, which contains information about the dynamics of nuclear eigenstates. It is a complex function,  $C(t)$ , which can be expressed as  $C'(t) + iC''(t)$ . The semiclassical approach to estimating correlation functions allows us to avoid the tedious calculations of nuclear dynamics and fundamentally simplifies the modeling of optical responses without losing physical significance. However,  $C(t)$  itself is not suitable for numerical simulations, as it does not have a classical analog. To simulate the absorption spectrum, we need to work with  $\tilde{C}(\omega) = \tilde{C}'(\omega) + i\tilde{C}''(\omega)$ , which is the frequency domain version of  $C(t)$  and is related to  $C(t)$  through the Fourier transform. The real  $\tilde{C}'(\omega)$  and imaginary  $\tilde{C}''(\omega)$  parts of  $\tilde{C}(\omega)$  are not independent functions and connected with each other by the fluctuation–dissipation theorem. All simulations begin with the evaluation of  $\tilde{C}''(\omega)$ . This function is temperature independent and serves as a basic characteristic of the bath. Thus, the expression for  $C(t)$  in terms of  $\tilde{C}''(\omega)$  would be as follows:

$$C(t) = \int_{-\infty}^{\infty} d\omega \cos(\omega t) \coth(\beta\hbar\omega/2) \tilde{C}''(\omega) + i \int_{-\infty}^{\infty} d\omega \sin(\omega t) \tilde{C}'(\omega) \quad (9)$$

By plugging the expression (9) into (8), we can derive the formula for the lineshape function,  $g(t)$ , in terms of the real function  $\tilde{C}''(\omega)$ :

$$g(t) = \frac{1}{2\pi} \int_{-\infty}^{+\infty} d\omega \frac{1 - \cos\omega t}{\omega^2} \coth\left(\frac{\beta\hbar\omega}{2}\right) \tilde{C}''(\omega) - \frac{i}{2\pi} \int_{-\infty}^{+\infty} d\omega \frac{\sin(\omega t)}{\omega^2} \tilde{C}'(\omega), \quad (10)$$

where  $\beta = 1/kT$ , and  $T$  is a temperature. Thus, we obtained expressions (9) and (10) that depend on  $\tilde{C}''(\omega)$ . This function is a crucial element in the model, as it allows us to calculate the correlations of the electronic transition moment using a set of effective parameters that can be interpreted classically.

All carotenoids exhibit a broad absorption spectrum due to the interaction between electronic excitation and phonons of the molecular skeleton and protein surrounding. To account for these effects, one can use the multimode Brownian oscillator model [22]. According to this model, the system Hamiltonian (1) needs to be modified by adding a bath Hamiltonian:

$$H_{bath} = \sum_n \left[ \frac{p_n^2}{2m_n} + \frac{1}{2} m_n \omega_n^2 \left( x_n - \sum_j \frac{c_{nj} q_j}{m_n \omega_n^2} \right)^2 \right] \quad (11)$$

This equation describes the interaction between the system's vibrational modes and the effective mode of the environment represented by  $c_{nj}$ . Without going into the details of the mathematical manipulations, which can be found in [22], we present the final formula for calculating the spectral density, in which the microparameters from the Hamiltonians (2), (3), and (11) are transformed into a set of  $\{\omega_j, S_j, \gamma_j\}$ :

$$\tilde{C}_j''(\omega) = \sum_j \frac{\hbar}{2m_j} \frac{S_j \omega \gamma_j(\omega)}{(\omega_j^2 - \omega^2)^2 + \omega^2 \gamma_j^2(\omega)}, \quad (12)$$

where  $\omega_j$  is the frequency,  $\gamma_j$  is the damping factor and  $S_j$  is the Huang–Rhys factor for each vibrational mode. Thus, the final expression for absorption spectrum is

$$\sigma_{abs} = \frac{1}{\pi} \text{Re} \int_0^\infty dt e^{i(\omega - \Omega_{eg})t} e^{-g(t)}, \quad (13)$$

In addition to the electron–phonon coupling, it is necessary to take into account the effect of inhomogeneous broadening of the band caused by interaction with the protein environment. To do this, we can evaluate the influence of the lowest vibrational modes by introducing a search window in the range from 100 to 600  $\text{cm}^{-1}$  with a uniform step size of 100  $\text{cm}^{-1}$ . Finally, to calculate the spectrum, one has to evaluate Equation (12), then (9), (10), and (13).

## 2.2. Differential Evolution

The quantitative description of quantum effects in biological systems requires advanced optimization methods due to their complex structure. One such method is the DE algorithm designed to find the global optimum of functions with multiple variables. For this purpose, we considered the minimized function that represents the difference between the experimentally measured and calculated spectra. This function is given by

$$f(\mathbf{x}_i) = \frac{1}{N} \sum_{n=1}^N (I(\omega_n) - \sigma_{abs}(\omega_n, \mathbf{x}_i))^2, \quad (14)$$

where  $I(\omega_n)$  is the measured spectrum and  $\sigma_{abs}(\omega_n, \mathbf{x}_i^g)$  is the calculated spectrum.  $\mathbf{x}_i$  is a set of optimization parameters.  $N$  is the number of points in the spectra.

The mechanism of the DE search can be explained as follows [32,33]: At the beginning, DE sets the boundaries for the optimized parameters in the mathematical model. These boundaries can be determined based on the specific requirements of the problem. The search range for free parameters can be set based on the specifics of the task. In  $n$ -dimensional space, where  $n$  is the number of free parameters, a set of vectors are created to find the best solution that corresponds to the minimum value of the objective function. Then, through a series of operations such as mutation, crossover, and selection, these vectors are modified. At each generation, the best vector is selected, which will be used to create the vectors for the next generation. There are three basic ways to calculate the mutation vector:

$$\mathbf{v}_j^g = \mathbf{x}_{r0}^g + F(\mathbf{x}_{r1}^g - \mathbf{x}_{r2}^g) \quad (15)$$

$$\mathbf{v}_j^g = \mathbf{x}_{best}^g + F(\mathbf{x}_{r1}^g - \mathbf{x}_{r2}^g), \quad (16)$$

$$\mathbf{v}_j^g = \mathbf{x}_{r0}^g + F(\mathbf{x}_{best}^g - \mathbf{x}_{r0}^g) + F(\mathbf{x}_{r1}^g - \mathbf{x}_{r2}^g), \quad (17)$$

where  $F \in [0, 1]$  is a weighting factor that affects the diversity of the mutant vectors.  $\mathbf{x}_{r0}^g$ ,  $\mathbf{x}_{r1}^g$ , and  $\mathbf{x}_{r2}^g$  are randomly selected vectors from the current population  $g$ ;  $\mathbf{x}_{best}^g$  is the best vector in this population. By performing a crossover operation, some coordinates from the mutation vector,  $\mathbf{v}_j^g$ , are replaced with the coordinates from one of the previous vectors with a certain probability  $Cr \in [0, 1]$ . After that, the best mutant vector is compared with

the current best vector, and the superior one becomes the new best solution and is added to the next population.

### 2.3. Computational Software

To model experimental data, we combined the procedures for calculating the optical response with the DE procedure in a single software package. The block diagram of the computational module is shown in Figure 2. The program input consists of files with DE parameters (strategy,  $F$ ,  $Cr$ , maximum number of generations), as well as parameters that define the conditions for simulating absorption spectra: the number of points in the time and frequency arrays, the step sizes in picosecond and inverse centimeters, ambient temperature, and the boundaries in the frequency domain where the experimental and theoretical spectra are compared. For the parameters of the semiclassical quantum model of a two-level electronic transition, the ability to change the status of whether this parameter is included in the optimization process is provided. Before starting the simulation, the population size is calculated based on a list of parameters that need to be adjusted.

The module of monomeric pigment optical response simulation comprises four stages, in which the spectral density (Equation (12)), correlation function (Equation (9)), lineshape function (Equation (10)), and absorption spectrum (Equation (13)) are calculated sequentially. This module is called by the DE procedure every time the optimization algorithm evaluates the fitness of a theoretical spectrum calculated for a specific mutant vector  $\mathbf{v}_j^g$ . Optimization ends when the stopping criterion is met, and either the maximum number of generations has been reached, or  $f(\mathbf{x}_i)$  become less than a specified value. The algorithm and software used to model and optimize the spectra are described in detail in our previous publications [15,16]. All procedures were written in C++; the MKL library was used to accelerate calculations with matrices and arrays.

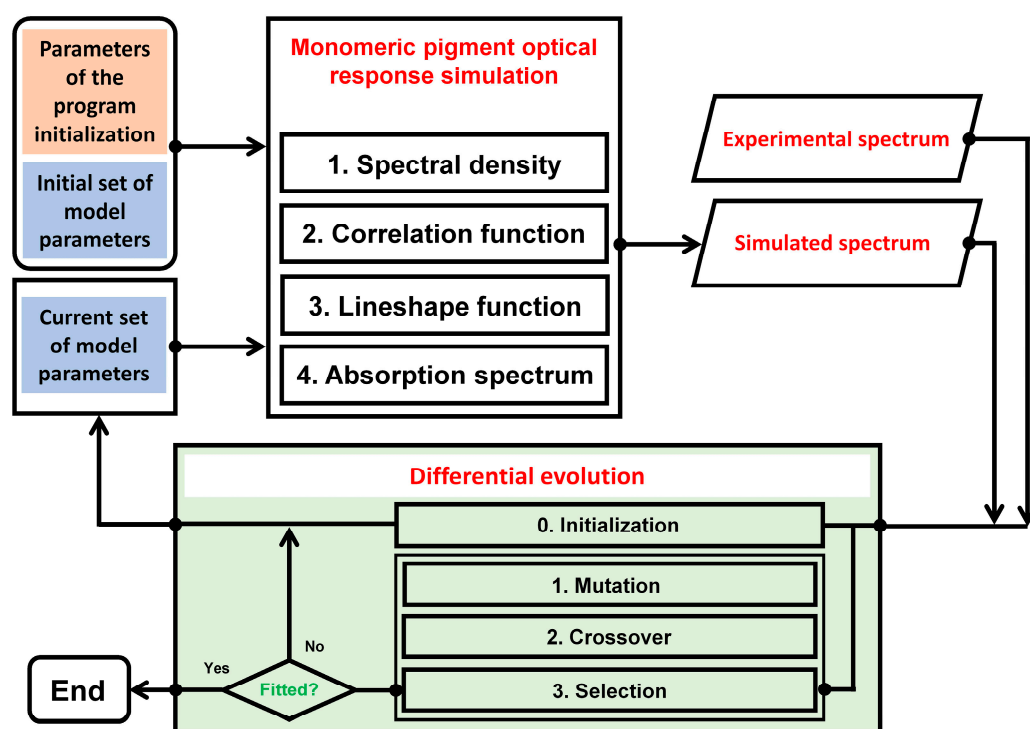
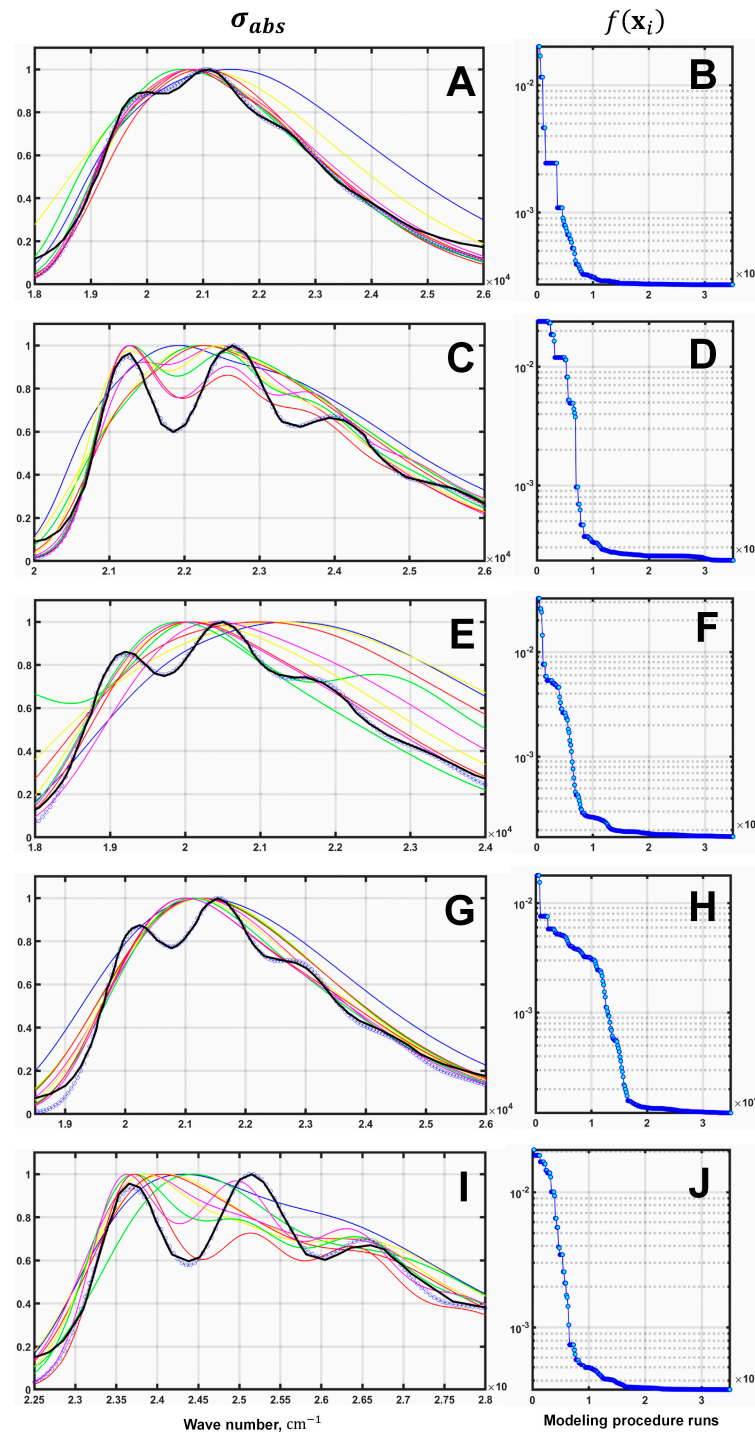


Figure 2. A block diagram of the software used to simulate the optical properties of organic pigments.

### 3. Results

The results of the optimization are presented in Figures 3–5. In these simulations, we modified the method of estimating the spectral density. From Equation (12), it follows that this function depends on the triplets  $\{\omega_j, S_j, \gamma_j\}$ , which characterize the  $j$ th vibrational

mode. Here,  $\omega_j$  are 13 fixed values determined as follows: low-frequency modes range from  $100\text{ cm}^{-1}$  to  $600\text{ cm}^{-1}$  with a uniform step of  $100\text{ cm}^{-1}$ ; then there are four effective modes corresponding to hydrogen bond wagging ( $\nu_4$ ), methyl rocking ( $\nu_3$ ), and vibrations of single ( $\nu_2$ ) and double ( $\nu_1$ ) carbon bonds. Their energies are  $965\text{ cm}^{-1}$ ,  $1006\text{ cm}^{-1}$ ,  $1158\text{ cm}^{-1}$ , and  $1524\text{ cm}^{-1}$ ; there are also three overtones with energies of  $2316\text{ cm}^{-1}$ ,  $2682\text{ cm}^{-1}$ , and  $3048\text{ cm}^{-1}$  which correspond to  $2\nu_2$ ,  $\nu_1 + \nu_2$ ,  $2\nu_1$ .



**Figure 3.** Fitting of neurosporaxanthin (A), neurosporene (C), torulene (E),  $\gamma$ -carotene (G), and  $\zeta$ -carotene (I) absorption by DE. Color lines are simulated spectra of the first ten generations. The black line is the experiment. Blue lines with markers are the best spectra obtained after 300 generations. Dynamics of the corresponding objective functions are shown in (B,D,F,H,J).

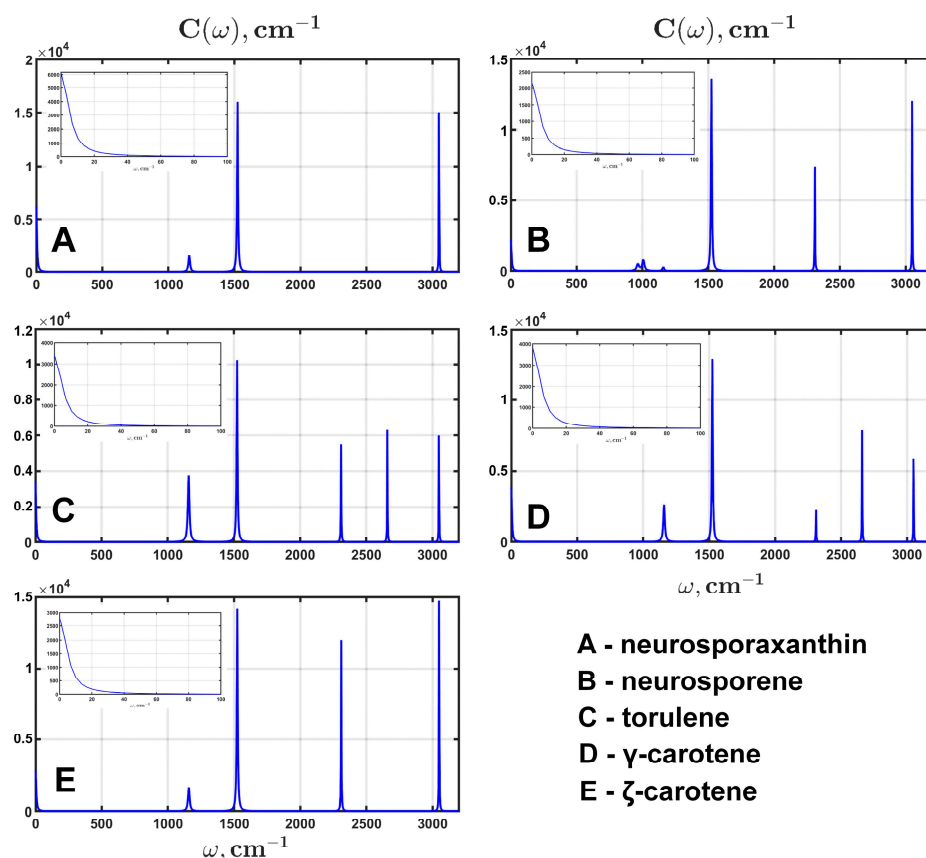


**Figure 4.** The spectral densities for the best-fitting neurosporaxanthin (A), neurosporene (B), torulene (C),  $\gamma$ -carotene (D), and  $\zeta$ -carotene (E) absorption spectra. Insets show the contribution of the low-frequency modes (from 0  $\text{cm}^{-1}$  to 100  $\text{cm}^{-1}$ ) in the spectral density.

The  $S_j$  values are adjusted during the optimization process, and  $\gamma_j$  are damping factors that depend on frequency  $\gamma_j = \gamma_j(\omega)$ . These factors were set as follows:  $\gamma_{2\nu_2} = 2 \text{ cm}^{-1}$  for the mode with the highest energy (3048  $\text{cm}^{-1}$ ); for other frequencies  $\gamma_j$  were estimated using the inverse-square relationship  $\gamma_j = \gamma_{2\nu_1} (\omega_{2\nu_1} / \omega_j)^2$ . These spectral density parameters are collected in Table 1. In addition to  $\{\omega_j, S_j, \gamma_j\}$ , the energy of  $|S_0\rangle \rightarrow |S_2\rangle$  electronic transition,  $\Omega_{\text{eg}}^0$ , was also a free parameter for optimization. Therefore, the total number of free parameters was 14. To evaluate Equations (9), (10), and (13), the time and frequency scales were calculated using  $2^{12}$  points.

These factors were set as follows: for the mode with the highest energy (3048  $\text{cm}^{-1}$ )  $\gamma_{2\nu_2} = 2 \text{ cm}^{-1}$ . For other frequencies,  $\gamma_j$  were estimated by the inverse-square dependence  $\gamma_j = \gamma_{2\nu_1} (\omega_{2\nu_1} / \omega_j)^2$ . All parameters of the spectral density are collected together in Table 1. In addition to  $\{\omega_j, S_j, \gamma_j\}$ , the energy of  $|S_0\rangle \rightarrow |S_2\rangle$  electronic transition  $\Omega_{\text{eg}}^0$  was also a free parameter for optimization. Thus, the total number of free parameters was 14. To evaluate Equations (9) and (12), the time and frequency scales were calculated with  $2^{12}$  points.

All simulations were conducted with the following settings for DE: *DE/best/1/exp* strategy,  $F = 0.6$ , and  $Cr = 0.95$ , with a population size of 140, and the number of generations was 300. The best results from 10 independent DE runs for each spectrum are represented in Figure 3. Table 2 shows the mean values of the free parameters and their standard deviations from 10 runs. Target function  $f(\mathbf{x}_i)$  characterizes the discrepancy between the measured and simulated spectra. All data obtained after 10 runs of DE are included in the Supplementary Materials. The spectral densities of the best fits are displayed in Figure 4, with an inset for each graph showing the spectral density between 0 and 100  $\text{cm}^{-1}$ . It is evident that the contribution from lower frequencies was limited to approximately 60  $\text{cm}^{-1}$ .



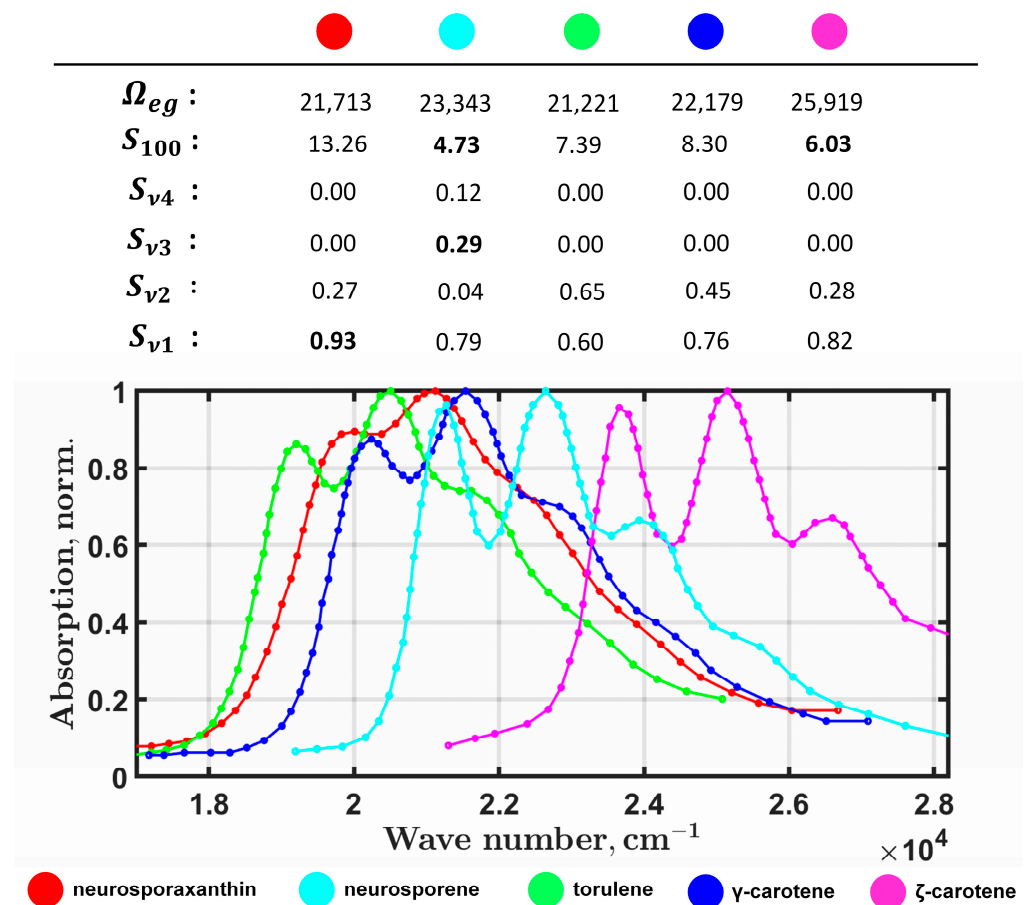


**Figure 5.** The effect of the electron–phonon interaction on the lineshapes of the absorption spectra. For carotenoids with weak inhomogeneous broadening, the contributions of  $\nu_3$  and  $\nu_4$  are statistically significant.

**Table 1.** Parameters of the generalized spectral density that are fixed during the optimization of the spectra.

$\omega_j, \text{cm}^{-1}$	100	200	300	400	500	600	965	1006	1158	1524	2316	2682	3048
$\gamma_j, \text{cm}^{-1}$	1858.1	464.5	206.5	116.1	74.3	51.6	20.0	18.4	13.9	8.0	3.5	2.6	2.0

**Table 2.** Parameters of the multimode Brownian oscillator model for neurosporaxanthin, neurosporene, torulene, γ-carotene, and ζ-carotene obtained after DE optimization.

	Neurosporaxanthin		Neurosporene		Torulene		γ-Carotene		ζ-Carotene	
	Mean	SD	Mean	SD	Mean	SD	Mean	SD	Mean	SD
$\Omega_{eg}$	21,712.6	0.4	23,342.5	4.1	21,221.1	3.1	22,179.2	5.7	25,918.9	3.1
$S_{100}$	13.26	$7.7 \times 10^{-3}$	4.73	0.02	7.39	0.03	8.30	0.03	6.03	0.01
$S_{200}$	$1.5 \times 10^{-3}$	$2.8 \times 10^{-3}$	$2.6 \times 10^{-3}$	$5.3 \times 10^{-3}$	$2.5 \times 10^{-4}$	$3.0 \times 10^{-4}$	$6.7 \times 10^{-4}$	$1.4 \times 10^{-3}$	$4.8 \times 10^{-4}$	$3.2 \times 10^{-4}$
$S_{300}$	$1.9 \times 10^{-4}$	$4.3 \times 10^{-4}$	$1.4 \times 10^{-5}$	$1.4 \times 10^{-5}$	$5.0 \times 10^{-5}$	$5.9 \times 10^{-5}$	$2.0 \times 10^{-4}$	$4.4 \times 10^{-4}$	$4.5 \times 10^{-4}$	$8.2 \times 10^{-4}$
$S_{400}$	$4.4 \times 10^{-5}$	$7.9 \times 10^{-5}$	$1.4 \times 10^{-5}$	$2.1 \times 10^{-5}$	$4.1 \times 10^{-5}$	$6.5 \times 10^{-5}$	$2.8 \times 10^{-5}$	$3.4 \times 10^{-5}$	$7.4 \times 10^{-5}$	$1.1 \times 10^{-4}$
$S_{500}$	$6.0 \times 10^{-5}$	$9.6 \times 10^{-5}$	$4.1 \times 10^{-5}$	$6.2 \times 10^{-5}$	$5.8 \times 10^{-6}$	$7.5 \times 10^{-6}$	$1.1 \times 10^{-5}$	$1.5 \times 10^{-5}$	$9.8 \times 10^{-5}$	$2.1 \times 10^{-4}$
$S_{600}$	$6.1 \times 10^{-6}$	$7.1 \times 10^{-6}$	$1.0 \times 10^{-5}$	$1.7 \times 10^{-5}$	$3.7 \times 10^{-5}$	$7.3 \times 10^{-5}$	$1.4 \times 10^{-5}$	$1.6 \times 10^{-5}$	$3.0 \times 10^{-5}$	$4.1 \times 10^{-5}$
$S_{v4}$	$4.9 \times 10^{-5}$	$6.5 \times 10^{-5}$	0.12	0.11	$4.5 \times 10^{-5}$	$7.5 \times 10^{-5}$	$3.7 \times 10^{-4}$	$1.1 \times 10^{-3}$	$9.6 \times 10^{-4}$	$2.6 \times 10^{-3}$
$S_{v3}$	$8.5 \times 10^{-5}$	$9.7 \times 10^{-5}$	0.29	0.14	$4.2 \times 10^{-4}$	$1.2 \times 10^{-3}$	$2.1 \times 10^{-5}$	$4.1 \times 10^{-5}$	$3.4 \times 10^{-3}$	$9.1 \times 10^{-3}$
$S_{v2}$	0.27	$2.5 \times 10^{-3}$	0.04	0.04	0.65	$6.8 \times 10^{-3}$	0.45	0.01	0.28	0.02
$S_{v1}$	0.93	$2.1 \times 10^{-3}$	0.79	0.01	0.60	$7.4 \times 10^{-3}$	0.76	0.01	0.82	$7.9 \times 10^{-3}$
$S_{2v2}$	$9.9 \times 10^{-6}$	$2.2 \times 10^{-5}$	0.09	$2.1 \times 10^{-3}$	0.06	0.01	0.02	0.01	0.14	$3.5 \times 10^{-3}$
$S_{v1+v2}$	$1.3 \times 10^{-6}$	$1.5 \times 10^{-6}$	$9.7 \times 10^{-5}$	$1.8 \times 10^{-4}$	0.05	0.02	0.08	0.02	$2.0 \times 10^{-5}$	$4.8 \times 10^{-5}$
$S_{2v1}$	0.13	$3.1 \times 10^{-4}$	0.10	$1.1 \times 10^{-3}$	0.06	0.01	0.04	0.01	0.13	$1.9 \times 10^{-3}$
$f(x)$	$2.7 \times 10^{-4}$		$2.3 \times 10^{-4}$		$1.7 \times 10^{-4}$		$1.2 \times 10^{-4}$		$3.4 \times 10^{-4}$	

It should be noted that during the modeling of the spectra of neurosporene and  $\zeta$ -carotene, after 10 runs of the program, we recorded 2–3 cases when the DE algorithm hit local minima. The values of the model parameters found in these cases were very different from those obtained in the other runs and did not agree with theoretical expectations. Additionally, the minimized function  $f(\mathbf{x}_i)$  in these cases was about 10 times higher and the obtained spectra did not visually correspond well with the experimental data. To obtain more reliable results, additional runs of the program were conducted for these spectra in order to avoid getting stuck in local minima. Considering that no further instances of hitting local minima occurred during the modeling of the remaining three spectra, it can be concluded that the developed method has sufficient robustness.

#### 4. Discussion

The main feature of the obtained model parameters was the high precision with which they were determined by the fitting procedure. The specified limit of 300 DE generations allowed for minimizing the objective function for all five spectra. The objective function dynamics (Figure 3) show that after 200 generations, the best agreement between the simulated and experimental data was achieved, but the next 100 generations of evolution were necessary to stabilize the model parameters. Interestingly, the lineshape of the calculated spectrum underwent the strongest changes during the first few dozen generations of evolution; then, the algorithm actually smoothed out some small parts of the profile.

Results in Table 2 show that the proposed semiclassical model converged to essentially the same final parameters regardless of the random initialization before each DE run. This was mainly due to the proper choice of the set of vibrational modes on the basis of which the spectral density was calculated. For example, to take the effects of the local environment (inhomogeneous broadening) on the optical response into account, six vibrational modes from 100 to 600  $\text{cm}^{-1}$  were considered when evaluating the spectral density (Table 1). Hypothetically, each of these modes would contribute to the broadening of the spectrum having non-zero  $S_j$ ; however, optimization revealed that only the lowest mode with  $\omega_j = 100 \text{ cm}^{-1}$  contributed to the spectral density. The Huang–Rhys factors of the other five modes tended to zero. If one compares  $S_{100}$  and the absorption linehapes for different carotenoids, the following pattern is found. Spectra with a pronounced band structure (neurosporene and  $\zeta$ -carotene) have smaller  $S_{100}$  compared with spectra with less pronounced ones. It is well known that Raman and IR spectroscopy of carotenoids do not detect signals within the range of 100 to 600  $\text{cm}^{-1}$  [18], which allows us to conclude that the effectiveness of our optimization method was confirmed through the simulation of carotenoid absorption spectra.

The modeling revealed that only neurosporene showed a significant contribution for the four modes associated with the oscillation of specific chemical bonds ( $\nu_1$ ,  $\nu_2$ ,  $\nu_3$ , and  $\nu_4$ ). Huang–Rhys factors of the double and single carbon bonds,  $S_{\nu_1}$  and  $S_{\nu_2}$ , proved to be the key parameters determining the optical response. Each of these parameters is significantly different from each other; the highest value of  $S_{\nu_1}$  corresponds to the spectrum of neurosporaxanthin. It can be unambiguously stated that an increase in  $S_{\nu_1}$  leads to a loss of fine structure in the carotenoid spectra. It is also important to note that only neurosporene turned out to have non-zero for all four modes  $\nu_{1-4}$ . The contribution of  $\nu_4$  and  $\nu_3$  to the spectral density for all other carotenoids was significantly zero (Table 2, Figure 5).

It appeared that overtones of the vibrational modes played an essential role in the modeling. For example, Huang–Rhys factors for  $2\nu_1$  overtone were found to be non-zero for all spectra.  $S_{\nu_1+\nu_2}$  is non-zero only for two spectra of torulene and  $\gamma$ -carotene.  $S_{2\nu_1}$  is, in general, much smaller than  $S_{\nu_1}$  and  $S_{\nu_2}$  for all carotenoids, but its contribution to the spectral density was significant (Table 2). This is due to the fact that in the equation for spectral density (12), the numerator was the product  $S_j \omega \gamma_j(\omega)$ , which means that the larger the frequency, the more intense was its contribution to  $\tilde{C}_j''(\omega)$ . Figure 4 shows the calculated spectral densities for the best fit after optimization. The contribution of

the  $\nu_1$  mode and its overtone  $2\nu_1$  was dominant for all carotenoids. There was a study in which the absorption of different carotenoids was modeled using the semiclassical quantum theory [25]. Only  $\nu_1$  and  $\nu_2$  modes of the spectral density were used to calculate the spectra (without considering overtones), and no optimization of the modeling was carried out. This resulted in all calculated spectra having the same issue—a discrepancy with the experimental data in the high-frequency region.

It is interesting to analyze the Huang–Rhys factors of the effective vibrational modes obtained by modeling the optical response with the peculiarities of the chemical structure of pigments. In addition to the main structural element, the polyene chain, carotenoids may contain terminal groups, the functional roles of which are related to stabilization of the molecule in pigment–protein complexes and lipid membranes, as well as modification of the linear optical response. Neurosporene and  $\zeta$ -carotene have no terminal groups and their spectra differ from the other three carotenoids in our study by the presence of a lineshape fine structure and narrower spectrum width. The fitting showed that  $S_{100}$  has lower values for these molecules than for pigments with terminal groups. In any case, it can be argued that terminal groups lead to broadening and smoothing of the  $|S_0\rangle \rightarrow |S_2\rangle$  electronic transition in carotenoids. Moreover, the presence of two different terminal groups (as in neurosporoxanthin) corresponds to the highest intensity for the vibrational mode with frequency  $\omega_j = 100 \text{ cm}^{-1}$ .

## 5. Conclusions

Considering the modeling of absorption spectra of neurosporaxanthin, neurosporene, torulene,  $\gamma$ -carotene, and  $\zeta$ -carotene as an example, it has been shown that the combined implementation of the differential evolution algorithm and semiclassical quantum simulation allows for the classification and analysis of the optical properties of organic pigments in solvents. For each pigment, the electronic transition spectrum was modeled within the framework of the multimode Brownian oscillator theory. As a result, we obtained spectral density functions that reveal effective electron–phonon interaction energies for vibrational modes ranging from  $100 \text{ cm}^{-1}$  to  $3000 \text{ cm}^{-1}$ . Analysis of the Huang–Rhys factors of the best-fitting models indicates that optical responses with weak inhomogeneous broadening, such as that exhibited by neurosporene, has pronounced contribution of the methyl rocking ( $\nu_3$ ) mode. In contrast, the spectra with strong inhomogeneous broadening results in a dominant contribution of the double carbon bonds ( $\nu_1$ ). Pigments with well-defined fine structures have lower values of Huang–Rhys factors for the low-frequency mode ( $\omega_j = 100 \text{ cm}^{-1}$ ). It is noteworthy that the largest value of  $S_j$  for  $\nu_1$  was obtained for neurosporaxanthin, whose molecular structure has the maximum asymmetry (two different terminal groups).

By analyzing the spectra of pigments found in pathogenic organisms using the above-mentioned method of optical response modeling, it is possible to create a database that includes both the spectra of the pigment in different solvents and the calculated parameters of the spectral density function. This method will allow us to distinguish vibrational frequencies in the spectral density of a pigment that do not change significantly in response to the external environment and those that are specific to a given environment. This classification of frequencies can then be used to analyze the other spectra not included in the database, and to determine whether they belong to a particular type of pigment. This database can be used for early detection of crop infestation, both through remote sensing and through the examination of samples washed from the surface of the grains.

**Supplementary Materials:** The following supporting information can be downloaded at: <https://www.mdpi.com/article/10.3390/math12233844/s1>, Tables S1 and S2: The results of DE modeling for neurosporaxanthin absorption; Tables S3 and S4: The results of DE modeling for neurosporene absorption; Tables S5 and S6: The results of DE modeling for torulene absorption; Tables S7 and S8: The results of DE modeling for  $\gamma$ -carotene absorption; Tables S9 and S10: The results of DE modeling for  $\zeta$ -carotene absorption.

**Author Contributions:** Supervision, conceptualization, software, writing—review and editing R.Y.P.; writing—review and editing, software, investigation, D.D.C.; software, investigation, V.A.K.; validation, formal analysis, visualization, investigation, A.P.R.; formal analysis, investigation, A.A.G.; conceptualization, methodology, S.V.G.; conceptualization, methodology, visualization, A.S.D.; funding acquisition, A.Y.I. All authors have read and agreed to the published version of the manuscript.

**Funding:** This research was funded by a grant of the Ministry of Science and Higher Education of the Russian Federation for large scientific projects in priority areas of scientific and technological development (subsidy identifier 075-15-2024-540).

**Data Availability Statement:** No additional data available.

**Conflicts of Interest:** The authors declare no conflicts of interest. The funders had no role in the design of the study; in the collection, analyses, or interpretation of data; in the writing of the manuscript; or in the decision to publish the results.

## References

- Gudkov, S.V.; Sarimov, R.M.; Astashev, M.E.; Pishchalnikov, R.Y.; Yanykin, D.V.; Simakin, A.V.; Shkirin, A.V.; Serov, D.A.; Konchekov, E.M.; Gusein-Zade, N.G.; et al. Modern physical methods and technologies in agriculture. *Physics-Uspekhi* **2024**, *67*, 194–210. [\[CrossRef\]](#)
- Zubler, A.V.; Yoon, J.-Y. Proximal methods for plant stress detection using optical sensors and machine learning. *Biosensors* **2020**, *10*, 193. [\[CrossRef\]](#) [\[PubMed\]](#)
- Mirkovic, T.; Ostroumov, E.E.; Anna, J.M.; van Grondelle, R.; Govindjee; Scholes, G.D. Light absorption and energy transfer in the antenna complexes of photosynthetic organisms. *Chem. Rev.* **2017**, *117*, 249–293. [\[CrossRef\]](#) [\[PubMed\]](#)
- Nielsen, M.R.; Sørensen, T.; Pedersen, T.B.; Westphal, K.R.; Díaz Fernández De Quincoces, L.; Sondergaard, T.E.; Wimmer, R.; Brown, D.W.; Sørensen, J.L. Final piece to the fusarium pigmentation puzzle—Unraveling of the phenalenone biosynthetic pathway responsible for perithecial pigmentation in the fusarium solani species complex. *Fungal Genet. Biol.* **2024**, *174*, 103912. [\[CrossRef\]](#) [\[PubMed\]](#)
- Elkhateeb, W.; Daba, G. Fungal pigments: Their diversity, chemistry, food and non-food applications. *Appl. Microbiol.* **2023**, *3*, 735–751. [\[CrossRef\]](#)
- Silva, F.H.C.A.; Wijewardane, N.K.; Bheemanahalli, R.; Raja Reddy, K.; Zhang, X.; Vennam, R.R. Comparison of uv, visible and near-infrared, and mid-infrared spectrometers to estimate maize and sorghum leaf nutrients using dry-intact and ground leaves. *Comput. Electron. Agric.* **2023**, *211*, 108001. [\[CrossRef\]](#)
- Matveyeva, T.A.; Sarimov, R.M.; Simakin, A.V.; Astashev, M.E.; Burmistrov, D.E.; Lednev, V.N.; Sdvizhenskii, P.A.; Grishin, M.Y.; Pershin, S.M.; Chilingaryan, N.O. Using fluorescence spectroscopy to detect rot in fruit and vegetable crops. *Appl. Sci.* **2022**, *12*, 3391. [\[CrossRef\]](#)
- Moskovskiy, M.N.; Sibirev, A.V.; Gulyaev, A.A.; Gerasimenko, S.A.; Borzenko, S.I.; Godyaeva, M.M.; Noy, O.V.; Nagaev, E.I.; Matveeva, T.A.; Sarimov, R.M. Raman spectroscopy enables non-invasive identification of mycotoxins p. Fusarium of winter wheat seeds. *Photonics* **2021**, *8*, 587. [\[CrossRef\]](#)
- Jones, R.R.; Hooper, D.C.; Zhang, L.; Wolverson, D.; Valev, V.K. Raman techniques: Fundamentals and frontiers. *Nanoscale Res. Lett.* **2019**, *14*, 231. [\[CrossRef\]](#)
- Parra-Rivero, O.; Paes de Barros, M.; Prado, M.d.M.; Gil, J.-V.; Hornero-Méndez, D.; Zacarías, L.; Rodrigo, M.J.; Limón, M.C.; Avalos, J. Neurosporaxanthin overproduction by fusarium fujikuroi and evaluation of its antioxidant properties. *Antioxidants* **2020**, *9*, 528. [\[CrossRef\]](#)
- Westphal, K.R.; Wollenberg, R.D.; Herbst, F.-A.; Sørensen, J.L.; Sondergaard, T.E.; Wimmer, R. Enhancing the production of the fungal pigment aurofusarin in fusarium graminearum. *Toxins* **2018**, *10*, 485. [\[CrossRef\]](#)
- Frandsen, R.J.N.; Rasmussen, S.A.; Knudsen, P.B.; Uhlig, S.; Petersen, D.; Lysøe, E.; Gottfredsen, C.H.; Giese, H.; Larsen, T.O. Black perithecial pigmentation in fusarium species is due to the accumulation of 5-deoxybostrycoidin-based melanin. *Sci. Rep.* **2016**, *6*, 26206. [\[CrossRef\]](#) [\[PubMed\]](#)
- Frandsen, R.J.N.; Nielsen, N.J.; Maolanon, N.; Sørensen, J.C.; Olsson, S.; Nielsen, J.; Giese, H. The biosynthetic pathway for aurofusarin in fusarium graminearum reveals a close link between the naphthoquinones and naphthopyrones. *Mol. Microbiol.* **2006**, *61*, 1069–1080. [\[CrossRef\]](#) [\[PubMed\]](#)
- Medentsev, A.G.; Arinbasarova, A.Y.; Akimenko, V.K. Biosynthesis of naphthoquinone pigments by fungi of the genus fusarium. *Appl. Biochem. Microbiol.* **2005**, *41*, 503–507. [\[CrossRef\]](#)
- Pishchalnikov, R.Y.; Chesalin, D.D.; Kurkov, V.A.; Shkirina, U.A.; Laptinskaya, P.K.; Novikov, V.S.; Kuznetsov, S.M.; Razjivin, A.P.; Moskovskiy, M.N.; Dorokhov, A.S.; et al. A prototype method for the detection and recognition of pigments in the environment based on optical property simulation. *Plants* **2023**, *12*, 4178. [\[CrossRef\]](#) [\[PubMed\]](#)
- Chesalin, D.D.; Kulikov, E.A.; Yaroshevich, I.A.; Maksimov, E.G.; Selishcheva, A.A.; Pishchalnikov, R.Y. Differential evolution reveals the effect of polar and nonpolar solvents on carotenoids: A case study of astaxanthin optical response modeling. *Swarm Evol. Comput.* **2022**, *75*, 101210. [\[CrossRef\]](#)

17. Blankenship, R.E. *Molecular Mechanisms of Photosynthesis*; Wiley: Hoboken, NJ, USA, 2008; pp. 1–321.
18. Hashimoto, H.; Uragami, C.; Yukihira, N.; Gardiner, A.T.; Cogdell, R.J. Understanding/unravelling carotenoid excited singlet states. *J. R. Soc. Interface* **2018**, *15*, 20180026. [[CrossRef](#)]
19. Hashimoto, H.; Uragami, C.; Cogdell, R.J. Carotenoids and photosynthesis. In *Carotenoids in Nature: Biosynthesis, Regulation and Function*; Stange, C., Ed.; Springer: New York, NY, USA, 2016; Volume 79, pp. 111–139.
20. Wei, T.; Balevičius, V.; Polívka, T.; Ruban, A.V.; Duffy, C.D.P. How carotenoid distortions may determine optical properties: Lessons from the orange carotenoid protein. *Phys. Chem. Chem. Phys.* **2019**, *21*, 23187–23197. [[CrossRef](#)]
21. Renger, T. Semiclassical modified redfield and generalized forster theories of exciton relaxation/transfer in light-harvesting complexes: The quest for the principle of detailed balance. *J. Phys. Chem. B* **2021**, *125*, 6406–6416. [[CrossRef](#)]
22. Mukamel, S. *Principles of Nonlinear Optical Spectroscopy*; Oxford University Press: New York, NY, USA; Oxford, UK, 1995; Volume 6, p. 543.
23. Pishchalnikov, R.Y.; Shubin, V.V.; Razjivin, A.P. Spectral differences between monomers and trimers of photosystem i depend on the interaction between peripheral chlorophylls of neighboring monomers in trimer. *Phys. Wave Phenom.* **2017**, *25*, 185–195. [[CrossRef](#)]
24. Friedl, C.; Fedorov, D.G.; Renger, T. Towards a quantitative description of excitonic couplings in photosynthetic pigment-protein complexes: Quantum chemistry driven multiscale approaches. *Phys. Chem. Chem. Phys.* **2022**, *24*, 5014–5038. [[CrossRef](#)] [[PubMed](#)]
25. Uragami, C.; Saito, K.; Yoshizawa, M.; Molnar, P.; Hashimoto, H. Unified analysis of optical absorption spectra of carotenoids based on a stochastic model. *Arch. Biochem. Biophys.* **2018**, *650*, 49–58. [[CrossRef](#)] [[PubMed](#)]
26. Kumar, A.; Srivastava, S.; Kumar, V.; Kulshrestha, N. Application aspects of nature-inspired optimization algorithms. In *Nature-Inspired Optimization Algorithms and Soft Computing: Methods, Technology and Applications for Iots, Smart Cities, Healthcare and Industrial Automation*; Institution of Engineering and Technology: Stevenage, UK, 2023; pp. 53–83.
27. Liu, J.; Sarker, R.; Elsayed, S.; Essam, D.; Siswanto, N. Large-scale evolutionary optimization: A review and comparative study. *Swarm Evol. Comput.* **2024**, *85*, 101466. [[CrossRef](#)]
28. Pătrăușanu, A.; Florea, A.; Neghină, M.; Dicoiu, A.; Chiș, R. A systematic review of multi-objective evolutionary algorithms optimization frameworks. *Process* **2024**, *12*, 869. [[CrossRef](#)]
29. Mohapatra, P.; Roy, S.; Das, K.N.; Dutta, S.; Raju, M.S.S. A review of evolutionary algorithms in solving large scale benchmark optimisation problems. *Intern. J. Math. Oper. Res.* **2022**, *21*, 104–126. [[CrossRef](#)]
30. Katoch, S.; Chauhan, S.S.; Kumar, V. A review on genetic algorithm: Past, present, and future. *Multimed. Tools Appl.* **2021**, *80*, 8091–8126. [[CrossRef](#)]
31. Abualigah, L.; Sheikhan, A.; Ikotun, A.M.; Zitar, R.A.; Alsoud, A.R.; Al-Shourbaji, I.; Hussien, A.G.; Jia, H. Particle swarm optimization algorithm: Review and applications. In *Metaheuristic Optimization Algorithms: Optimizers, Analysis, and Applications*; Elsevier: Amsterdam, The Netherlands, 2024; pp. 1–14.
32. Storn, R. System design by constraint adaptation and differential evolution. *IEEE Trans. Evol. Comput.* **1999**, *3*, 22–34. [[CrossRef](#)]
33. Storn, R.; Price, K. Differential evolution—A simple and efficient heuristic for global optimization over continuous spaces. *J. Glob. Optim.* **1997**, *11*, 341–359. [[CrossRef](#)]
34. Carrasco, J.; García, S.; Rueda, M.M.; Das, S.; Herrera, F. Recent trends in the use of statistical tests for comparing swarm and evolutionary computing algorithms: Practical guidelines and a critical review. *Swarm Evol. Comput.* **2020**, *54*, 100665. [[CrossRef](#)]
35. Trinkunas, G.; Holzwarth, A.R. Kinetic modeling of exciton migration in photosynthetic systems. 3. Application of genetic algorithms to simulations of excitation dynamics in three-dimensional photosystem core antenna reaction center complexes. *Biophys. J.* **1996**, *71*, 351–364. [[CrossRef](#)]
36. Raszewski, G.; Saenger, W.; Renger, T. Theory of optical spectra of photosystem ii reaction centers: Location of the triplet state and the identity of the primary electron donor. *Biophys. J.* **2005**, *88*, 986–998. [[CrossRef](#)] [[PubMed](#)]
37. Trinkunas, G.; Connelly, J.P.; Muller, M.G.; Valkunas, L.; Holzwarth, A.R. Model for the excitation dynamics in the light-harvesting complex ii from higher plants. *J. Phys. Chem. B* **1997**, *101*, 7313–7320. [[CrossRef](#)]
38. Bruggemann, B.; Sznee, K.; Novoderezhkin, V.; van Grondelle, R.; May, V. From structure to dynamics: Modeling exciton dynamics in the photosynthetic antenna ps1. *J. Phys. Chem. B* **2004**, *108*, 13536–13546. [[CrossRef](#)]
39. Ahmad, M.F.; Isa, N.A.M.; Lim, W.H.; Ang, K.M. Differential evolution: A recent review based on state-of-the-art works. *Alex. Eng. J.* **2022**, *61*, 3831–3872. [[CrossRef](#)]
40. Hornero-Méndez, D.; Limón, M.C.; Avalos, J. Hplc analysis of carotenoids in neurospora xanthin-producing fungi. In *Methods in Molecular Biology*; Humana Press Inc.: Totowa, NJ, USA, 2018; Volume 1852, pp. 269–281.
41. Cambaza, E.; Koseki, S.; Kawamura, S. The use of colors as an alternative to size in fusarium graminearum growth studies. *Foods* **2018**, *7*, 100. [[CrossRef](#)]
42. Cambaza, E. Comprehensive description of fusarium graminearum pigments and related compounds. *Foods* **2018**, *7*, 165. [[CrossRef](#)]
43. Moreira, L.M.; Lyon, J.P.; Lima, A.; Codognoto, L.; Machado, A.E.; Tiago, F.d.S.; Araújo, D.M.; Silva, E.L.; Hioka, N.; Rodrigues, M.R. Quinqueangulin and rubrofusarin: A spectroscopy study. *Orbital Electron. J. Chem.* **2017**, *9*, 290–298. [[CrossRef](#)]



44. Ávalos Cordero, F.J.; Pardo-Medina, J.; Parra-Rivero, O.; Ruger-Herreros, M.M.; Rodríguez-Ortiz, L.R.; Hornero-Méndez, D.; Limon, M.C. Carotenoid biosynthesis in fusarium. *J. Fungi* **2017**, *3*, 39. [[CrossRef](#)]
45. Avalos, J.; Prado-Cabrero, A.; Estrada, A.F. Neurosporaxanthin production by neurospora and fusarium. *Microb. Carotenoids Fungi Methods Protoc.* **2012**, *898*, 263–274.

**Disclaimer/Publisher’s Note:** The statements, opinions and data contained in all publications are solely those of the individual author(s) and contributor(s) and not of MDPI and/or the editor(s). MDPI and/or the editor(s) disclaim responsibility for any injury to people or property resulting from any ideas, methods, instructions or products referred to in the content.